Geometrical information based imaging of a high-contrast scattering object

Denis Vautrin, Jérôme Idier, Nicolas Paul

Geometrical information based imaging of a high-contrast scattering object

D. Vautrin[a*], J. Idier[a] and N. Paul[b]

[a] Institut de Recherche en Communications et Cybernétique de Nantes, 1 rue de la Noë, 44321 Nantes, France
[b] Electricité De France, Recherche et Développement, Département STEP, 6 quai Watier, 78400 Chatou, France

Abstract

This paper is devoted to the resolution of an inverse scattering problem. Such problems are known to be highly nonlinear and ill-posed. In our case, the reconstruction is rendered all the more difficult by the high contrast: the physical characteristics of the scattering object greatly differ from those of the surrounding medium. To properly counterbalance the ill-posedness of the problem, an original shape model taking into account precise prior information about the geometry of the scattering object is proposed. Moreover, the scatterer shape is described with a reduced number of variables and the parametrization enables one to solve the inverse problem with a gradient-based algorithm. This contributes to reduce the computation cost. Tests conducted on synthetic datasets reveal good performance of the proposed algorithm, contrary to more classical approaches based on a Tikhonov regularization scheme or the use of an edge-preserving penalization function.

Introduction

The efficient resolution of inverse scattering problems has gained much interest in the last decade. Today, it finds applications in numerous areas such as biomedical imaging, non destructive testing or geophysical exploration. Its goal is to extract information such as the location, shape and physical characteristics of an object from measurements of a wavefield scattered by this object. Inverse scattering problems are known to be highly ill-posed [1]. In general, this is mainly due to the nonlinear relation between the measurements and the underground characteristics, the large scale of the problem and the limited amount of measured data: sensors are usually in small number and cannot be located all around the object under test.

The ill-posedness of the problem is also influenced by the contrast, i.e. the difference in the physical characteristics between the scattering object and the surrounding medium. In case of very low contrast, a linear approximation of the wavefield propagation model can be used [2, 3]. For higher contrasts, scattering effects cannot be neglected and the nonlinearities of the model must be taken into account. In this case, several methods can be used for the resolution of the inverse problem. Some are based on iterative minimization of quadratic criterions such as:

- the Born iterative method and the distorted Born iterative method [4, 5]. They rely on successive linearization of the model,
- the modified gradient method [6]. This method estimates the scattered wavefield as well as the probed medium characteristics but involves the relaxation of constraints in the model,
- the contrast source inversion method (CSI) [7]. It is similar to the modified gradient method except that the so-called contrast source is estimated instead of the scattered wavefield.

*E-mail: denis.vautrin@edf.fr. Present address: Electricité De France, Recherche et Développement, Département STEP, 6 quai Watier, 78400 Chatou, France

The latter methods are advantageous from a computational standpoint but they involve some approximations in the model. Other methods consist in minimizing directly a least-square criterion where the nonlinearity of the model is explicitly taken into account [8, 9, 10].

In this article, we are interested in the determination of the shape of transmission overhead line structure foundations with a seismic imaging technique. The wavelengths of the probing waves are known to be of the same order of magnitude as the foundations dimensions, and the physical characteristics of foundations greatly differ from those of the earth [11]. In this case, scattering effects must be taken into account to achieve an accurate imaging of the subsurface [12, 13]. To avoid any approximation in the model, the inversion is performed by minimizing a nonquadratic least-square criterion. This implies the possible presence of local minima in the criteria. Global optimization algorithms could be considered to guarantee the convergence towards the global minimum but such approaches cannot be applied here because the computational effort would be prohibitive. A gradient-based iterative procedure is used, which is better suited to nonlinear large-scale problems.

In the framework of seismic imaging, the contrast can be defined as the ratio of the velocity in the scattering object to the velocity in the surrounding medium. In the application considered in [14], the velocity values in the subsurface range from $\sim$3000 m.s^{-1} to $\sim$3500 m.s^{-1}, which corresponds to a contrast value of about 1.2. This enables the authors to use the Born approximation. In [15, 16], the contrasts are higher and the nonlinearity is taken into account. In [15], the velocities range from 1500 m.s^{-1} to 5500 m.s^{-1}, which corresponds to a contrast value of about 3.7, and the inversion is performed with the CSI method. In [16], the velocities range from 700 m.s^{-1} to 3500 m.s^{-1}, which corresponds to a contrast value of about 5, and inversion is performed by minimizing a non-quadratic cost function.

A challenging aspect of the application considered here is the very high contrast value. In some situations, it is expected to be greater than 10. In such cases, the contrast is so large that a lack of sensitivity of the criterion appears, which results in a significant slow down of the inversion procedure. In [17], we proposed to circumvent the problem with a logarithmic variable substitution technique. A synthetic configuration of small size was considered and to regularize the problem, the minimized criterion was penalized with a smooth approximation of the total variation. We showed that the change of variables resulted in a significant acceleration of the inversion process. However, on a configuration of realistic size, this technique is not efficient enough to produce an accurate result in terms of the geometry of the foundation. A pitfall of the algorithm is that the regularization scheme does not include information about the scatterer shape.

In this article, an inversion procedure based on a segmentation of the probed medium into two complementary areas is proposed. The goal is to determine the shape of the boundary separating the two areas as well as the spatial distributions of the physical characteristics inside each area. The proposed inversion scheme is advantageous from several points of view. Strong prior information concerning the shape of the scatterer is taken into account. The main assumption is that foundations are all in one piece and horizontally convex. Moreover, the scatterer shape is described with a reduced number of parameters and the parametrization enables one to optimize all the unknowns jointly by means of a gradient-based algorithm. This is well suited to large-scale nonlinear problems and contributes to reduce the computation cost.

This paper is organized as follows. In section 1, the context of the problem at hand is presented. In particular, we show on a configuration of reduced size that in our case, two regularization techniques commonly used in seismic imaging fail to determine the shape of the scatterer. In section 2, the proposed inversion procedure is presented. The prior assumptions are listed and the proposed shape model is explained. In section 3, reconstruction results from synthetic data are presented. We show that the proposed inversion scheme is more efficient both in terms of reconstruction accuracy and computation time. The robustness of the algorithm to uncertainty on some assumptions is also assessed and a configuration of real size is considered.

1 Statement of the problem

1.1 Description of the measurement procedure

A seismic imaging technique is used to probe the underground medium [11]. A seismic wave is generated using a vibrator and measurements of the scattered wavefield of particle velocity are collected on the

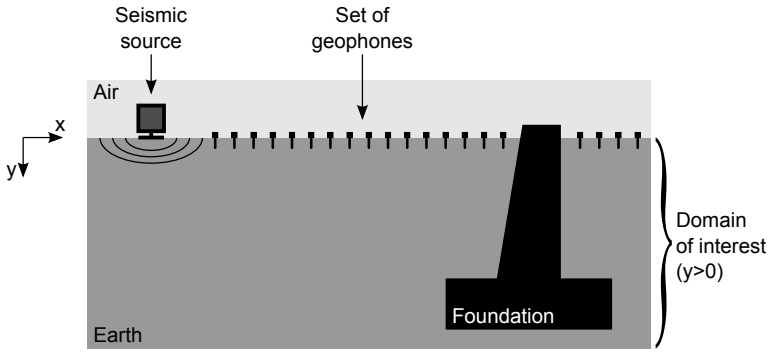

Figure 1: Scheme of the seismic imaging setup

ground surface with geophones (about a hundred in practice), as illustrated on figure 1. To collect more information, the measurement procedure is repeated for multiple locations of the source. We limit ourselves to the two-dimensional case because the computation cost would be prohibitive for a three-dimensional imaging. The measurement system is thus placed along a line, roughly in the plane of symmetry of the foundation, and the medium characteristics are assumed invariant along the orthogonal axis.

1.2 Statement of the inverse problem

The aim of the inverse problem is to determine the underground physical characteristics knowing the acquisition procedure (i.e. the successive locations of the source, the signal emitted by the source and the locations of the receivers) and the measurements. Let us stress that data are recorded from the surface only, with a limited number of geophones, and only the vertical component of the particle velocity is measured. This tends to increase the underdetermined nature of the problem.

We solve the inverse problem by minimizing a regularized least-squares cost function. In the context of seismic imaging, this approach was initiated by Tarantola during the 1980s [18]. The inversion is performed in the frequency domain. Let us suppose that for frequency ω and source location k, the measured data set $\boldsymbol{y}_{\omega,k}$ is related to the unknowns (gathered in $\boldsymbol{\theta}$) as follows:

$$\boldsymbol{y}_{\omega,k} = \boldsymbol{g}_{\omega,k}(\boldsymbol{\theta}) + \boldsymbol{\eta}_{\omega,k} \tag{1}$$

where $\boldsymbol{g}_{\omega,k}$ is the output of the forward model and $\boldsymbol{\eta}_{\omega,k}$ is white Gaussian noise. The *maximum a posteriori* estimate is obtained by minimizing the cost function:

$$\mathcal{J}(\boldsymbol{\theta}) = \sum_{\omega} \sum_{k} \|\boldsymbol{y}_{\omega,k} - \boldsymbol{g}_{\omega,k}(\boldsymbol{\theta})\|^2 + \gamma\phi(\boldsymbol{\theta}) \tag{2}$$

where ϕ is a regularization term. Its role is to introduce prior information into the inversion process in order to counterbalance the ill-posedness of the problem. The choice of the regularization technique plays an essential role in the performance of the inversion procedure. The free parameter γ is a weighting hyperparameter which remains fixed during the inversion. In our tests, its value is set heuristically by visually comparing the estimated velocity maps and the exact solution.

In practice, we consider a small number of frequencies ω. The amount of data to be processed is thus considerably reduced, which contributes to reduce the computation cost. This approach is commonly adopted in seismic waveform inversion [19, 20].

1.3 Resolution of the forward problem

An efficient algorithm of resolution of the forward problem is a prerequisite for the inversion. The aim of the forward problem is to compute a synthetic set of data at a reasonable cost. The underground characteristics and the acquisition procedure (i.e. the successive locations of the source, the signal emitted by the source and the locations of the receivers) are assumed known.

A model developed by the STEP department of EDF R&D [21] is used. It is based on the linear elastic wave equations. The forward problem is solved in the frequency domain, which allows to restrict to selected frequencies during the inversion process. It has also an algorithmic advantage since a number of computational operations depend on the frequency, but not on the source location. In the frequency domain, the propagation equations are:

$$\begin{aligned} -i\omega F^x_{\omega,k} = \omega^2 \rho V^x_{\omega,k} &+ \frac{\partial}{\partial x}\left(\rho v_{\mathrm{p}}^2 \frac{\partial V^x_{\omega,k}}{\partial x} + \rho\left(v_{\mathrm{p}}^2 - 2v_{\mathrm{s}}^2\right)\frac{\partial V^y_{\omega,k}}{\partial y}\right) \\ &+ \frac{\partial}{\partial y}\left(\rho v_{\mathrm{s}}^2 \frac{\partial V^x_{\omega,k}}{\partial y} + \rho v_{\mathrm{s}}^2 \frac{\partial V^y_{\omega,k}}{\partial x}\right) \end{aligned} \tag{3}$$

$$\begin{aligned} -i\omega F^y_{\omega,k} = \omega^2 \rho V^y_{\omega,k} &+ \frac{\partial}{\partial x}\left(\rho v_{\mathrm{s}}^2 \frac{\partial V^x_{\omega,k}}{\partial y} + \rho v_{\mathrm{s}}^2 \frac{\partial V^y_{\omega,k}}{\partial x}\right) \\ &+ \frac{\partial}{\partial y}\left(\rho\left(v_{\mathrm{p}}^2 - 2v_{\mathrm{s}}^2\right)\frac{\partial V^x_{\omega,k}}{\partial x} + \rho v_{\mathrm{p}}^2 \frac{\partial V^y_{\omega,k}}{\partial y}\right) \end{aligned} \tag{4}$$

where $F^x_{\omega,k}$ and $F^y_{\omega,k}$ correspond to the horizontal and vertical components of the force density. They are directly deduced from the source location and the source signal. $V^x_{\omega,k}$ and $V^y_{\omega,k}$ correspond to the horizontal and vertical components of the particle velocity. v_{p}, v_{s} and ρ are the underground characteristics. They denote the pressure-wave velocity, the squared shear-wave velocity, and the density respectively.

These equations are discretized with a finite-difference scheme on two staggered grids using the so-called Saenger stencil [22]. The propagation equations can then be written as a linear matrix relation:

$$\boldsymbol{F}_{\omega,k} = \mathbf{A}_\omega \boldsymbol{V}_{\omega,k} \tag{5}$$

$\mathbf{A}_\omega$ is the impedance matrix which depends linearly on three vectors $\boldsymbol{v}_p^2$, $\boldsymbol{v}_s^2$ and $\boldsymbol{\rho}$ which respectively gather the squared pressure-wave velocity v_{p}^2, the squared shear-wave velocity v_{s}^2, and the density ρ, at any point of the mesh. In order to speed up the resolution of the forward problem, $\mathbf{A}_\omega$ is computed using sparse matrices [23]:

$$\mathbf{A}_\omega = \mathbf{H}^p_\omega \mathbf{Diag}\left\{\boldsymbol{v}_{\mathrm{p}}^2 \odot \boldsymbol{\rho}\right\} \mathbf{G}^p_\omega + \sum_{i=1}^{3} \mathbf{H}^s_{\omega,i} \mathbf{Diag}\left\{\boldsymbol{v}_{\mathrm{s}}^2 \odot \boldsymbol{\rho}\right\} \mathbf{G}^s_{\omega,i} + \omega^2 \mathbf{Diag}\left\{\mathbf{H}^\rho \boldsymbol{\rho}\right\} \tag{6}$$

where $\mathbf{G}^p_\omega$, $\mathbf{H}^p_\omega$, $\mathbf{G}^s_{\omega,i}$, $\mathbf{H}^s_{\omega,i}$ and $\mathbf{H}^\rho$ are sparse matrices corresponding to finite-difference operators. The nonzeros values are equal to $\frac{1}{2\Delta x}$ or $\frac{1}{2\Delta y}$, where Δx and Δy are the horizontal and vertical step sizes, except on the edges where boundary conditions called Perfectly Matched Layers are introduced in order to work on a finite spatial domain [24]. $\odot$ denotes the componentwise product, and $\mathbf{Diag}\{\boldsymbol{w}\}$ is a diagonal matrix with $\boldsymbol{w}$ as the main diagonal.

To compute a synthetic data set, $\boldsymbol{V}_{\omega,k}$ is computed by solving the linear system (5) and the measurements are extracted using a sampling matrix $\mathbf{E}_{\mathrm{g}}$:

$$\boldsymbol{g}_{\omega,k} = \mathbf{E}_{\mathrm{g}} \mathbf{A}_\omega^{-1} \boldsymbol{F}_{\omega,k} \tag{7}$$

All types of waves are involved in equation (7) including reflected, refracted, scattered, converted, surface waves and multiples. Our work thus takes place in the full-waveform inversion (FWI) framework, contrary to many common seismic imaging techniques such as seismic reflection, seismic refraction or travel time tomography.

1.4 Inversion tests using two common regularization techniques

Few research results have been reported in the context of elastic FWI [25, 26]. Specifically, let us mention [13, 25, 26, 27]. More applications of FWI have been performed under the acoustic approximation [19, 28, 29, 30, 31]. Two regularization schemes are commonly used in FWI: (1) a Tikhonov regularization scheme, which is closely connected to the Bayesian framework pioneered by Tarantola in the geophysical inversion context [18], and (2) an edge-preserving regularization scheme corresponding to a smooth

Table 1: Characteristic values of the earth, concrete and air areas

Concrete	Earth	Air
$v_{\mathrm{p}}^{\mathrm{C}} = 4000$ m.s^{-1}	$v_{\mathrm{p}}^{\mathrm{E}} = 300$ m.s^{-1}	$v_{\mathrm{p}}^{\mathrm{A}} = 0$ m.s^{-1}
$v_{\mathrm{s}}^{\mathrm{C}} = 2200$ m.s^{-1}	$v_{\mathrm{s}}^{\mathrm{E}} = 150$ m.s^{-1}	$v_{\mathrm{s}}^{\mathrm{A}} = 0$ m.s^{-1}
$\rho^{\mathrm{C}} = 1500$ kg.m^{-3}	$\rho^{\mathrm{E}} = 1500$ kg.m^{-3}	$\rho^{\mathrm{A}} = 1.2$ kg.m^{-3}

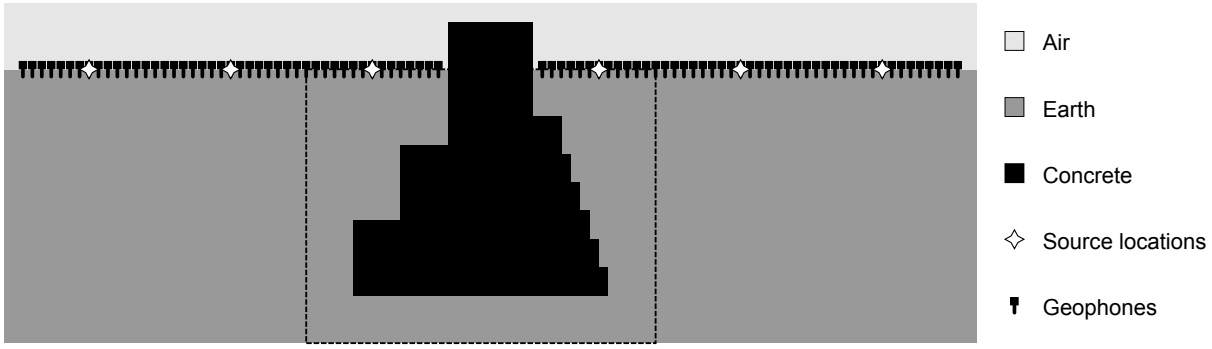

Figure 2: Scheme of the synthetic medium of reduced size. The dashed line delimits the zone of interest of size 74 cm $\times$ 58 cm.

approximation of total variation [32]. The reader can refer to [33] for a very complete development of this second technique in the geophysical inversion context.

In this subsection, these two regularization schemes are applied on a synthetic configuration. The scattering object considered here is of reduced size but it is close to our final application in terms of contrast. We show that the inversion process fails in determining the shape of the scatterer with the two considered regularization techniques. Indeed, they do not incorporate precise prior information about the probed medium to properly counterbalance the ill-posedness of the problem.

1.4.1 Configuration description

The underground medium size is 2 meters and 0.7 meters in horizontal and vertical directions. It is discretized with a spatial resolution $\Delta x = \Delta y = 2$ centimeters. It includes a concrete structure of about 0.5 meters in width and in height. Table 1 lists the characteristic values in each region. The seismic source takes six successive locations. It produces a vertical force represented by a 2-D Gaussian with a standard deviation of Δx and Δy along the x- and y-axis respectively. The source signal is a 200 Hz Ricker wavelet. 10 frequencies equally distributed in the bandwidth are selected for the inversion (from 100 Hz to 500 Hz). 90 geophones are used for the measurements. Figure 2 presents a scheme of the probed medium and the seismogram corresponding to the second position of the source on the left side of the foundation is shown in figure 3. In order to avoid a situation of *inverse crime*, white Gaussian noise is added to the simulated data (the signal to noise ratio is equal to 30 dB).

To reduce the computation cost, the underground characteristics are estimated only inside a region of interest. It is depicted by dashed lines in figure 2. Outside the region of interest, the characteristics are assumed known *a priori*. Furthermore, the contrast between earth and concrete characteristics is known to be very high for v_{p} and v_{s} (the corresponding ratio is greater than 13) but not for ρ (the ratio is less than 2). To reduce the computation cost while preserving the contrast, the density ρ is assumed constant in the subsurface and only the distributions of v_{p} and v_{s} remain unknown, as in [26, 34].

1.4.2 Inversion with a Tikhonov regularization scheme

Generally speaking, a Tikhonov regularization function corresponds to a quadratic penalty term either applied to the velocities themselves, or to differences between velocity values at neighbouring pixels. Here, we suppose that the characteristic values of earth are known *a priori* and ϕ penalizes the squared difference to the earth characteristics at each pixel.

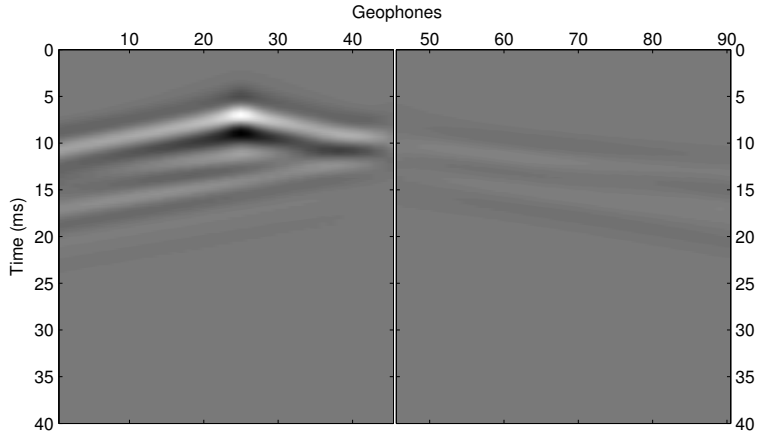

Figure 3: Seismogram corresponding to the second position of the source on the left side of the foundation. It represents the vertical particle velocity measured by each geophone in the temporal domain.

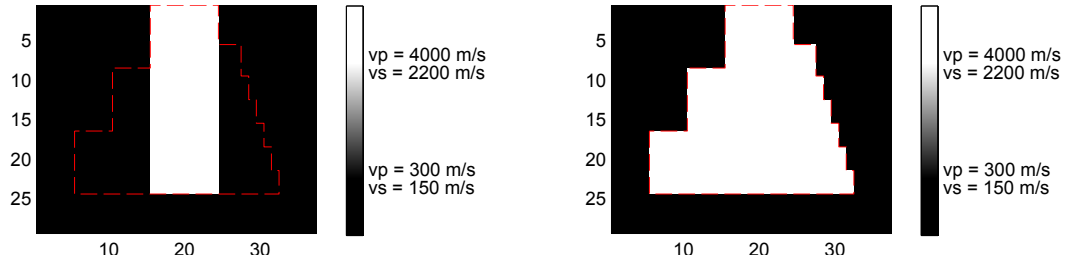

Figure 4: Two initializations of the algorithm are considered: either the top of the scatterer is extended down to the foundation depth (left), or the underground characteristics are set to the exact solution (right).

In [17], it is shown that the inversion process can be drastically accelerated with a logarithmic change of variables. The minimized criterion is thus written as a function of $\boldsymbol{\chi}_\mathrm{p}$ and $\boldsymbol{\chi}_\mathrm{s}$ which respectively gather the logarithm of v_p and v_s at any point of the mesh, and the following regularization function is adopted:

$$\phi(\boldsymbol{\chi}_\mathrm{p}, \boldsymbol{\chi}_\mathrm{s}) = \sum_n \left([\boldsymbol{\chi}_\mathrm{p}]_n - \log v_\mathrm{p}^\mathrm{E}\right)^2 + \left([\boldsymbol{\chi}_\mathrm{s}]_n - \log v_\mathrm{s}^\mathrm{E}\right)^2 \tag{8}$$

Following [35, 36], the data are introduced progressively during the inversion procedure. Starting from the lowest frequency data, groups of frequencies of growing size are considered in the summation over ω in (2). It is only when the current criterion is properly minimized (in the sense of a stopping criterion) that a new frequency component is incorporated. The criterion is minimized by means of the L-BFGS algorithm [37]. This quasi-Newton method is based only on criterion and gradient computations. It is well suited to our large-scale nonlinear optimization problem since it requires a small amount of storage to approximate the Hessian.

Two distinct initializations described by figure 4 have been considered. For both cases, figure 5 presents the maps of characteristics v_p and v_s obtained after optimization as well as the temporal evolution of the criterion value. The presence of peaks in the temporal evolution of the criterion is due to the progressive introduction of the data during the inversion. Each increase of the criterion corresponds to the incorporation of a new frequency. It is followed by a decrease of the criterion, which is due to the minimization procedure. The results show that despite the large computation time, the Tikhonov approach completely fails to produce an accurate result in terms of the geometry of the foundation.

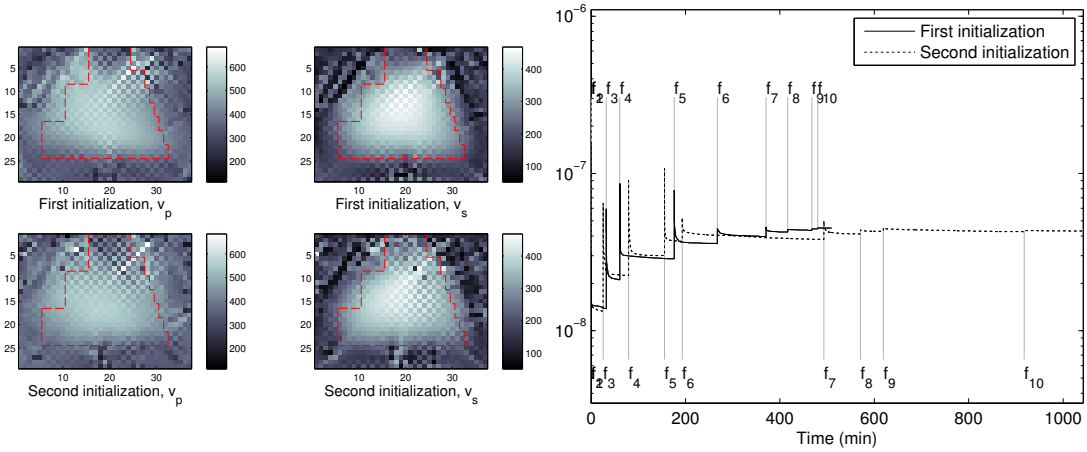

Figure 5: Results obtained with the Tikhonov regularization scheme, $\gamma = 10^{-10}$ (left: final maps of v_p and v_s for each initialization, right: temporal evolution of the criterion)

1.4.3 Inversion with an edge-preserving regularization scheme

An acknowledged drawback of the Tikhonov regularization scheme is to produce oversmoothed maps. In contrast, the second regularization scheme we tested better preserves sharp transitions between smooth regions. The following smooth approximation of the total variation is considered:

$$\phi(\boldsymbol{\chi}_\mathrm{p}, \boldsymbol{\chi}_\mathrm{s}) = \sum_{(m,n)\in\mathsf{C}} \sqrt{([\boldsymbol{\chi}_\mathrm{p}]_m - [\boldsymbol{\chi}_\mathrm{p}]_n)^2 + ([\boldsymbol{\chi}_\mathrm{s}]_m - [\boldsymbol{\chi}_\mathrm{s}]_n)^2 + \delta^2} \tag{9}$$

where C denotes the set of neighbouring pixels either in the horizontal or the vertical directions.

The results are presented on figure 6. The velocity maps are less smooth and the convergence is much faster than with the quadratic regularization, which may be explained by the fact that the edge-preserving penalization is better suited. However, they are still far from an accurate estimation of the true velocity maps. On the one hand, the regions corresponding to earth and concrete remain quite heterogeneous. On the other hand, the concrete characteristics are underestimated: the maximal values obtained are about $v_\mathrm{p} = 1200$ m.s^{-1} and $v_\mathrm{s} = 800$ m.s^{-1} instead of $v_\mathrm{p}^\mathrm{C} = 4000$ m.s^{-1} and $v_\mathrm{s}^\mathrm{C} = 2200$ m.s^{-1}. Finally, and most importantly for our application, the obtained geometry is a very rough approximation of the true one. Other penalization functions based on an L_2L_0 norm [38] can also be used. Compared to (9), they favour sharp transitions in a larger amount, since they tend towards a constant for large difference values instead of a linear growth regime. However, such functions are highly non convex, which makes the minimization of the resulting cost function more difficult. According to our tests, the results become strongly dependent on the initialization, without reaching the expected inversion quality.

2 Description of the proposed inversion scheme

2.1 Segmentation of the underground medium

We now describe the proposed inversion procedure. It is based on a segmentation of the underground medium into two complementary areas Ω^C and Ω^E separated by the boundary Γ. The two areas correspond to the inside and the outside of the foundation respectively. A vector of binary values is associated to each area:

$$\left[\boldsymbol{R}^\mathrm{C}(\Gamma)\right]_n = \begin{cases} 1 & \text{if mesh point } n \text{ belongs to } \Omega^\mathrm{C} \\ 0 & \text{if mesh point } n \text{ belongs to } \Omega^\mathrm{E} \end{cases} \tag{10}$$

$$\left[\boldsymbol{R}^\mathrm{E}(\Gamma)\right]_n = 1 - \left[\boldsymbol{R}^\mathrm{C}(\Gamma)\right]_n \tag{11}$$

Let us suppose that the characteristics of earth and concrete are known. Taking into account the logarithmic change of variables introduced in subsection 1.4, the unknown underground characteristics

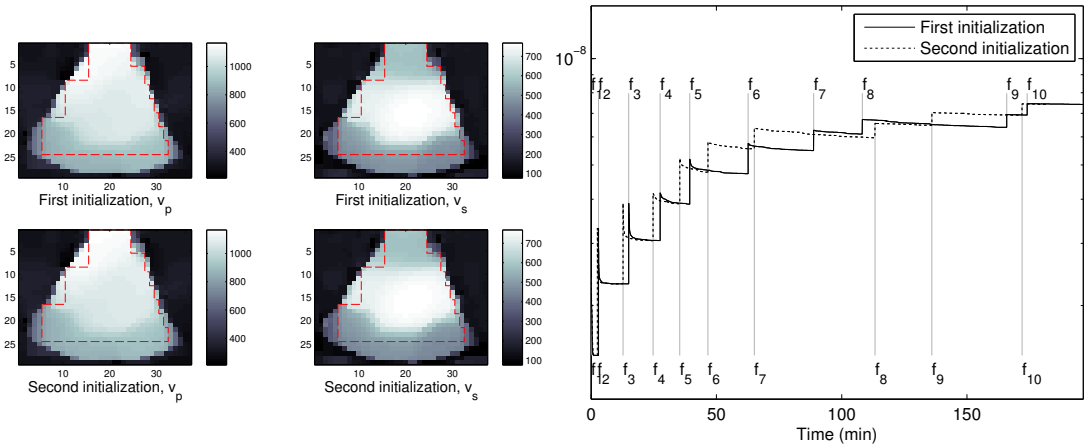

Figure 6: Results obtained with the edge-preserving regularization scheme, $\gamma = 10^{-11}$ and $\delta = 10^{-2}$ (left: final maps of v_p and v_s for each initialization, right: temporal evolution of the criterion)

are related to the outline of the foundation as follows:

$$\left[\boldsymbol{\chi}_\mathrm{p}(\Gamma)\right]_n = \left[\boldsymbol{\chi}_\mathrm{p}^\mathrm{C}\right]_n \left[\boldsymbol{R}^\mathrm{C}(\Gamma)\right]_n + \left[\boldsymbol{\chi}_\mathrm{p}^\mathrm{E}\right]_n \left[\boldsymbol{R}^\mathrm{E}(\Gamma)\right]_n \tag{12}$$

$$\left[\boldsymbol{\chi}_\mathrm{s}(\Gamma)\right]_n = \left[\boldsymbol{\chi}_\mathrm{s}^\mathrm{C}\right]_n \left[\boldsymbol{R}^\mathrm{C}(\Gamma)\right]_n + \left[\boldsymbol{\chi}_\mathrm{s}^\mathrm{E}\right]_n \left[\boldsymbol{R}^\mathrm{E}(\Gamma)\right]_n \tag{13}$$

where $\boldsymbol{\chi}_\mathrm{p}^\mathrm{C}$ and $\boldsymbol{\chi}_\mathrm{s}^\mathrm{C}$ (resp. $\boldsymbol{\chi}_\mathrm{p}^\mathrm{E}$ and $\boldsymbol{\chi}_\mathrm{s}^\mathrm{E}$) gather the logarithm of the concrete (resp. earth) velocities at any point of the mesh. The resulting penalized least-squares cost function depends on Γ according to:

$$\mathcal{J}(\Gamma) = \sum_\omega \sum_k \|\boldsymbol{y}_{\omega,k} - \boldsymbol{g}_{\omega,k} \circ \boldsymbol{m}(\Gamma)\|^2 + \phi(\Gamma) \tag{14}$$

where $\boldsymbol{m}$ is the shape model defined by (12) and (13).

2.2 Available prior information

To constrain the boundary, strong prior information is incorporated in the inversion procedure. Let us make the available prior information about the probed medium more explicit. It can be stated as a list of seven assumptions, **A1** to **A7**. The first five are linked to the general structure of foundations while the last two refer to information that can be obtained experimentally by means of complementary techniques:

A1 : A foundation is all in one piece.

A2 : Any horizontal cross-section of a foundation is rectangular. Given that we work in a plane of symmetry of the foundation, it is represented by a horizontal segment (figure 7).

A3 : A foundation has a flat basis.

A4 : The width of the foundation increases with depth.

A5 : The top of a foundation is visible.

A6 : The depth of the foundation can be estimated beforehand with an *impact-echo* method [39].

A7 : A prior estimate of the earth characteristics is available. More precisely, the pressure-wave velocity can be estimated by means of a seismic refraction technique and the shear-wave velocity can be deduced from the propagation of the surface waves [11]. The characteristics of concrete can be set to standard values.

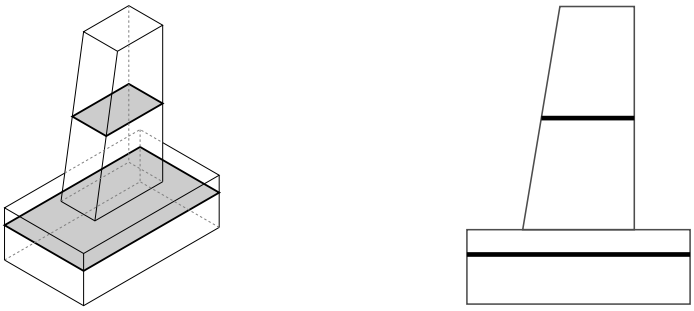

Figure 7: Representation of a foundation in 3-D (left). Any horizontal cross-section is rectangular. In the plane of symmetry (right), this corresponds to a horizontal segment.

The next question is how to parametrize the scatterer outline. In the framework of inverse scattering, two main approaches can be distinguished. On the one hand, some authors use a parametric shape model. The advantage of this approach is to work with a reduced number of descriptive parameters. For example, the scatterer outline can be described with polygons [40, 41], splines [42, 43], spherical harmonics [44] or radial basis functions [45]. On the other hand, a non-parametric method can be used. The scatterer outline is modelled as a deformable function. A typical example is the level-set approach introduced by Osher and Sethian [46, 47]. In this framework, the scatterer shape evolves more freely and topological changes such as merging or splitting are handled automatically. It has been applied to the resolution of inverse scattering problems in [48, 49, 50].

None of the latter two approaches is perfectly suited to the present context. On one side, no sufficient prior information is available to define a specific family of geometries. Indeed, a polygonal representation could be rather well suited, but the number of vertices should be known in advance. On the other side, the level-set would not enable to easily incorporate the geometrical assumptions listed above. In [51], a trade-off between the two approaches is proposed. The level-set formalism is used but the optimized shape is constructed by combining shapes of a predefined dictionary. One difficulty of this method is the determination of a shape dictionary consistent with the scatterer structure.

Here, a new parametrization taking into account the prior information about the scatterer shape is presented. The model we propose can be described as "semi-parametric" since a finite but large number of parameters is used.

2.3 Description of the scatterer shape

We first present the proposed parametrization in the continuous case.

Any horizontal cross-section is represented by a horizontal segment (**A2**). In other words, Ω^{C} is horizontally convex: for each couple of points (P_1, P_2) in Ω^{C} with $[P_1P_2]$ horizontal, any point of $[P_1P_2]$ belongs to Ω^{C}. Thus, any horizontal line crossing the foundation intersect the boundary Γ at exactly two points. At the ordinate $y = d$, their positions relative to any given vertical reference line $x = l_{\mathrm{ref}}$ are denoted by $l_l(d)$ and $l_r(d)$.

The whole boundary is thus described by two functions l_l and l_r. They are defined on $[0, D]$, where D is an estimate of the foundation depth (**A6**). The fact that a foundation is all in one piece (**A1**) and that it has a flat basis (**A3**) is thus implicitly taken into account. If the width of the foundation increases with depth (**A4**), l_l and l_r are two non-decreasing functions. This description is illustrated in figure 8.

Two 2-D binary functions R^{C} and R^{E} associated to Ω^{C} and Ω^{E} respectively (see (10) and (11)) are deduced from l_l and l_r:

$$R^{\mathrm{C}}(x,y) = \begin{cases} \mathcal{H}(x - l_{\mathrm{ref}} + l_l(y))\,(1 - \mathcal{H}(x - l_{\mathrm{ref}} - l_r(y))) & \text{if } 0 \le y \le D \\ 0 & \text{if } y > D \end{cases} \tag{15}$$

$$R^{\mathrm{E}}(x,y) = 1 - R^{\mathrm{C}}(x,y) \tag{16}$$

where $\mathcal{H}$ denotes the Heaviside function: $\mathcal{H}(x) = 1$ if $x \ge 0$, 0 if $x < 0$.

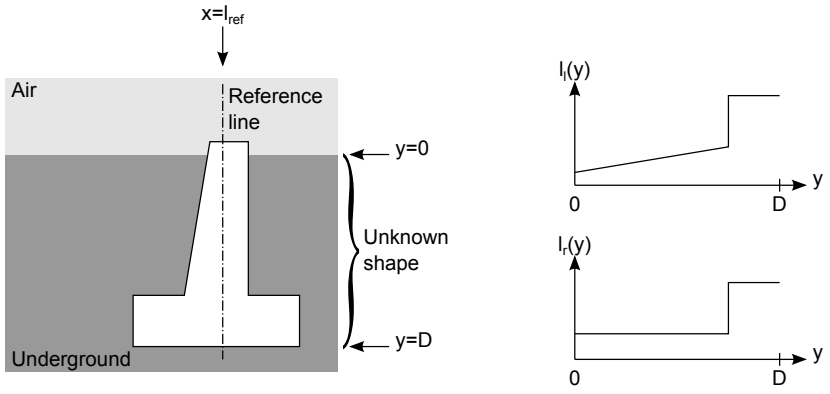

Figure 8: Description of the foundation shape. Left: scheme of the underground medium, right: corresponding functions l_l and l_r

In the discrete case, the foundation shape is described by two vectors $\boldsymbol{l}_l$ and $\boldsymbol{l}_r$ instead of functions l_l and l_r. Their number of entries is equal to the number of horizontal mesh lines partially covering the foundation. The vectors $\boldsymbol{R}^{\mathrm{C}}$ and $\boldsymbol{R}^{\mathrm{E}}$ are deduced from $\boldsymbol{l}_l$ and $\boldsymbol{l}_r$ using the Heaviside function as in the continuous case.

Using such a model, the whole prior information linked to the foundation geometry is taken into account. A reduced number of parameters are used compared to the level-set method, for which the number of variables used to describe the target outline is equal to the number of mesh points. Nonetheless, there is no additional restriction on the foundation geometry besides the assumptions listed above, as it would be the case with a parametric approach.

2.4 Inversion procedure

The exact velocity values of earth and concrete, introduced in (12) and (13), are not known in practice. Instead, we use a preliminary estimation of the earth and concrete characteristics (**A7**) but these estimates may not correspond to the real underground characteristics. Indeed, the preliminary estimation procedure tends to produce smooth velocity maps and thus may not take account of some heterogeneities. Moreover, a discrepancy between the estimated and the exact velocity values may exist. In order to be able to retrieve the exact characteristic values, space varying perturbations are added to the model described above. They are estimated during the inversion.

In the following, the preliminary estimations of the earth (resp. concrete) area characteristics are denoted by $\tilde{\boldsymbol{\chi}}_{\mathrm{p}}^{\mathrm{E}}$ and $\tilde{\boldsymbol{\chi}}_{\mathrm{s}}^{\mathrm{E}}$ (resp. $\tilde{\boldsymbol{\chi}}_{\mathrm{p}}^{\mathrm{C}}$ and $\tilde{\boldsymbol{\chi}}_{\mathrm{s}}^{\mathrm{C}}$) and the characteristics perturbations are denoted by $\boldsymbol{\varepsilon}_{\mathrm{p}}$ and $\boldsymbol{\varepsilon}_{\mathrm{s}}$. The list of unknowns to be determined is thus: $\boldsymbol{l}_l$, $\boldsymbol{l}_r$, $\boldsymbol{\varepsilon}_{\mathrm{p}}$ and $\boldsymbol{\varepsilon}_{\mathrm{s}}$. They are related to the underground characteristics as follows:

$$\boldsymbol{\chi}_{\mathrm{p}}(\boldsymbol{l}_l, \boldsymbol{l}_r, \boldsymbol{\varepsilon}_{\mathrm{p}}) = \tilde{\boldsymbol{\chi}}_{\mathrm{p}}^{\mathrm{C}} \odot \boldsymbol{R}^{\mathrm{C}}(\boldsymbol{l}_l, \boldsymbol{l}_r) + \tilde{\boldsymbol{\chi}}_{\mathrm{p}}^{\mathrm{E}} \odot \boldsymbol{R}^{\mathrm{E}}(\boldsymbol{l}_l, \boldsymbol{l}_r) + \boldsymbol{\varepsilon}_{\mathrm{p}} \tag{17}$$

$$\boldsymbol{\chi}_{\mathrm{s}}(\boldsymbol{l}_l, \boldsymbol{l}_r, \boldsymbol{\varepsilon}_{\mathrm{s}}) = \tilde{\boldsymbol{\chi}}_{\mathrm{s}}^{\mathrm{C}} \odot \boldsymbol{R}^{\mathrm{C}}(\boldsymbol{l}_l, \boldsymbol{l}_r) + \tilde{\boldsymbol{\chi}}_{\mathrm{s}}^{\mathrm{E}} \odot \boldsymbol{R}^{\mathrm{E}}(\boldsymbol{l}_l, \boldsymbol{l}_r) + \boldsymbol{\varepsilon}_{\mathrm{s}} \tag{18}$$

Without any additional regularization tool, let us stress that the estimation problem would be undetermined. Indeed, for any characteristics fields $\boldsymbol{\chi}_{\mathrm{p}}$ and $\boldsymbol{\chi}_{\mathrm{s}}$ and any values of the parameters $\boldsymbol{l}_l$ and $\boldsymbol{l}_r$, one can find $\boldsymbol{\varepsilon}_{\mathrm{p}}$ and $\boldsymbol{\varepsilon}_{\mathrm{s}}$ such that (17) and (18) are verified. Therefore, we propose to incorporate a weighted quadratic penalty term applied to $\boldsymbol{\varepsilon}_{\mathrm{p}}$ and $\boldsymbol{\varepsilon}_{\mathrm{s}}$ into the minimized cost function:

$$\mathcal{J}(\boldsymbol{l}_l, \boldsymbol{l}_r, \boldsymbol{\varepsilon}_{\mathrm{p}}, \boldsymbol{\varepsilon}_{\mathrm{s}}) = \sum_{\omega} \sum_{k} \|\boldsymbol{y}_{\omega,k} - \boldsymbol{g}_{\omega,k} \circ \boldsymbol{m}(\boldsymbol{l}_l, \boldsymbol{l}_r, \boldsymbol{\varepsilon}_{\mathrm{p}}, \boldsymbol{\varepsilon}_{\mathrm{s}})\|^2 + \gamma \left(\|\boldsymbol{\varepsilon}_{\mathrm{p}}\|^2 + \|\boldsymbol{\varepsilon}_{\mathrm{s}}\|^2 \right) \tag{19}$$

where $\boldsymbol{g}_{\omega,k}$ is the forward model (see subsection 1.3) and $\boldsymbol{m}$ is the shape model described by (17) and (18). The value of the weighting hyperparameter γ is set heuristically and remains fixed during the inversion. The tests we performed showed low sensitivity of the inversion results to the value of γ. Indeed, the regularizing effect is mainly due to the shape model itself rather than to the penalty terms of the criterion.

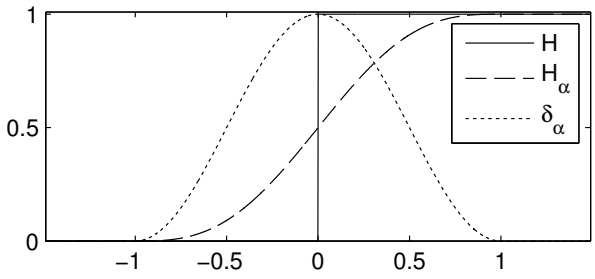

Figure 9: Approximation of the Heaviside function and its derivative

Therefore, in the framework of real data processing, we can assume that the value of γ will be fixed in advance and will not have to be tuned by the user.

The computation cost due to the use of the proposed shape model is negligible compared to the computation of $\boldsymbol{g}_{\omega,k}$. Moreover, the proposed regularization scheme enables one to optimize all the unknowns in a simultaneous way with a gradient-based technique. This contributes to perform the inversion efficiently. In contrast, in [41], a polygonal shape is optimized with a gradient-based technique but the vertices are updated one after the other. In [42, 43], the minimization technique does not benefit from gradient information. Our algorithm also has an advantage over the level-set method, for which the optimization procedure must regularly be stopped to perform an update of the descriptive variables [52, 53].

The shape model as defined by equations (15) to (18) is not differentiable: it involves the Heaviside function $\mathcal{H}$ which is discontinuous at zero. In practice, we propose to adopt a smoothed approximation of the Heaviside function $\mathcal{H}_\alpha$ that is usual within the level-set framework (see figure 9):

$$\mathcal{H}_\alpha(x) = \begin{cases} \frac{1}{2}\left(1 + \frac{x}{\alpha} + \frac{1}{\pi}\sin\frac{\pi x}{\alpha}\right) & \text{if } |x| \leq \alpha \\ 1 & \text{if } x > \alpha \\ 0 & \text{if } x < -\alpha \end{cases} \tag{20}$$

The shape derivative can thus be computed by means of the function δ_α :

$$\delta_\alpha(x) = \begin{cases} \frac{1}{2\alpha}\left(1 + \cos\frac{\pi x}{\alpha}\right) & \text{if } |x| \leq \alpha \\ 0 & \text{if } |x| > \alpha \end{cases} \tag{21}$$

The parameter α determines the length of the transition in $\mathcal{H}_\alpha$. It is set to the discretization step Δx as suggested in [53].

2.5 Estimation of the source signal

In this subsection, we show how our model can incorporate the estimation of the source signal following the procedure proposed in [13]. Indeed, experimental tests showed that the wave train propagating in the underground medium does not exactly match the signal generated by the seismic source. During its transmission to the underground medium, we observe that some frequencies are attenuated. Therefore, the source signal cannot be assumed perfectly known *a priori*.

For each source location k, let $\tilde{s}_k$ and s_k denote a first estimate of the source signal and the unknown exact source signal, respectively. Let us suppose that s_k is equal to the convolution output between $\tilde{s}_k$ and a filtering signal a_k, i.e.,

$$s_k(\omega) = a_k(\omega)\tilde{s}_k(\omega) \tag{22}$$

in the frequency domain.

For given source location k and frequency ω, the force density field (denoted by $\boldsymbol{F}_{\omega,k}$ in subsection 1.3) depends linearly on the amplitude of the signal source by construction and also depends linearly

on the simulated data set (see equation (7)). Let $\boldsymbol{g}_{\omega,k}$ and $\tilde{\boldsymbol{g}}_{\omega,k}$ denote the simulated data sets which correspond to the exact and the estimated source signals, respectively. We thus have:

$$\boldsymbol{g}_{\omega,k} = a_{\omega,k}\tilde{\boldsymbol{g}}_{\omega,k} \tag{23}$$

Therefore, estimating the source signal amounts to estimating the coefficients $a_{\omega,k}$. These additional unknowns are incorporated in the minimized criterion as follows:

$$\begin{aligned}\mathcal{J}(\boldsymbol{l}_l, \boldsymbol{l}_r, \boldsymbol{\varepsilon}_{\rm p}, \boldsymbol{\varepsilon}_{\rm s}, a_{\omega,k}) = \quad & \sum_\omega \sum_k \left\| \boldsymbol{y}_{\omega,k} - a_{\omega,k}\ \tilde{\boldsymbol{g}}_{\omega,k} \circ \boldsymbol{m}(\boldsymbol{l}_l, \boldsymbol{l}_r, \boldsymbol{\varepsilon}_{\rm p}, \boldsymbol{\varepsilon}_{\rm s}) \right\|^2 \\ & + \gamma \left(\|\boldsymbol{\varepsilon}_{\rm p}\|^2 + \|\boldsymbol{\varepsilon}_{\rm s}\|^2 \right)\end{aligned} \tag{24}$$

The latter criterion is quadratic with respect to $a_{\omega,k}$ when $\boldsymbol{l}_{\rm p}$, $\boldsymbol{l}_{\rm s}$, $\boldsymbol{\varepsilon}_{\rm p}$ and $\boldsymbol{\varepsilon}_{\rm s}$ are fixed. Thus, we can deduce an analytical expression for the optimal values of $a_{\omega,k}$:

$$a_{\omega,k} = \frac{(\tilde{\boldsymbol{g}}_{\omega,k} \circ \boldsymbol{m}(\boldsymbol{l}_l, \boldsymbol{l}_r, \boldsymbol{\varepsilon}_{\rm p}, \boldsymbol{\varepsilon}_{\rm s}))^\dagger \boldsymbol{y}_{\omega,k}}{\|\tilde{\boldsymbol{g}}_{\omega,k} \circ \boldsymbol{m}(\boldsymbol{l}_l, \boldsymbol{l}_r, \boldsymbol{\varepsilon}_{\rm p}, \boldsymbol{\varepsilon}_{\rm s})\|^2} \tag{25}$$

This expression can be incorporated into (24):

$$\begin{aligned}\mathcal{J}(\boldsymbol{l}_l, \boldsymbol{l}_r, \boldsymbol{\varepsilon}_{\rm p}, \boldsymbol{\varepsilon}_{\rm s}) = \quad & \sum_\omega \sum_k \left\| \boldsymbol{y}_{\omega,k} - \frac{(\tilde{\boldsymbol{g}}_{\omega,k} \circ \boldsymbol{m}(\boldsymbol{l}_l, \boldsymbol{l}_r, \boldsymbol{\varepsilon}_{\rm p}, \boldsymbol{\varepsilon}_{\rm s}))^\dagger \boldsymbol{y}_{\omega,k}}{\|\tilde{\boldsymbol{g}}_{\omega,k} \circ \boldsymbol{m}(\boldsymbol{l}_l, \boldsymbol{l}_r, \boldsymbol{\varepsilon}_{\rm p}, \boldsymbol{\varepsilon}_{\rm s})\|^2}\ \tilde{\boldsymbol{g}}_{\omega,k} \circ \boldsymbol{m}(\boldsymbol{l}_l, \boldsymbol{l}_r, \boldsymbol{\varepsilon}_{\rm p}, \boldsymbol{\varepsilon}_{\rm s}) \right\|^2 \\ & + \gamma \left(\|\boldsymbol{\varepsilon}_{\rm p}\|^2 + \|\boldsymbol{\varepsilon}_{\rm s}\|^2 \right)\end{aligned} \tag{26}$$

This way, the source signal is estimated without explicitly introducing additional unknowns.

3 Results

This section provides some numerical results that illustrate the efficiency of the proposed approach. Firstly, we consider the configuration of reduced size introduced in subsection 1.4 and we evaluate the improvement brought in comparison with the Tikhonov and the edge-preserving regularization schemes. The robustness to uncertainties on the foundation depth estimation (assumption **A6**) and on the earth characteristics estimation (assumption **A7**) is also tested. Secondly, results obtained on a configuration of realistic size are presented.

3.1 Comparison with the Tikhonov and the edge-preserving regularization schemes

The proposed algorithm is first applied on the configuration of reduced size presented in subsection 1.4. We assume that the foundation width increases with depth (assumption **A4**). Therefore, positivity constraints are applied on the components of $\boldsymbol{l}_l$ and $\boldsymbol{l}_r$. In practice, we resorted to the L-BFGS-B algorithm to minimize the criterion under positivity constraints [54]. L-BFGS-B is an efficient variant of the L-BFGS algorithm that accounts for bound constraints on the unknowns. The inversion was performed under the same conditions as previously and with the same initializations (see figure 4). The source signal was assumed known.

The results show that the foundation geometry is much better imaged here than with Tikhonov and the edge-preserving regularization schemes. At convergence, the foundation outline is very close to the exact solution. In particular, the straight sides of the foundation are well reconstructed, which was not the case with the edge-preserving regularization scheme.

Table 2 compares the computation times required by the three approaches. All tests were performed on a computer equipped with eight quad-core 3 GHz processors and 16 GB memory. The differences are significant: the proposed algorithm converges about two times faster than the edge-preserving regularization scheme, and from five to ten times faster than the Tikhonov regularization scheme.

3.2 Robustness of the algorithm

The proposed inversion procedure is based on the prior estimation of the foundation depth (assumption **A6**) and of the earth characteristics (assumption **A7**). These prior estimates are obtained by means of experimental procedures, which are subject to uncertainty. In this subsection, we evaluate how errors on these prior estimates impact the inversion results on the configuration of reduced size. Inversion is performed under the same conditions as previously.

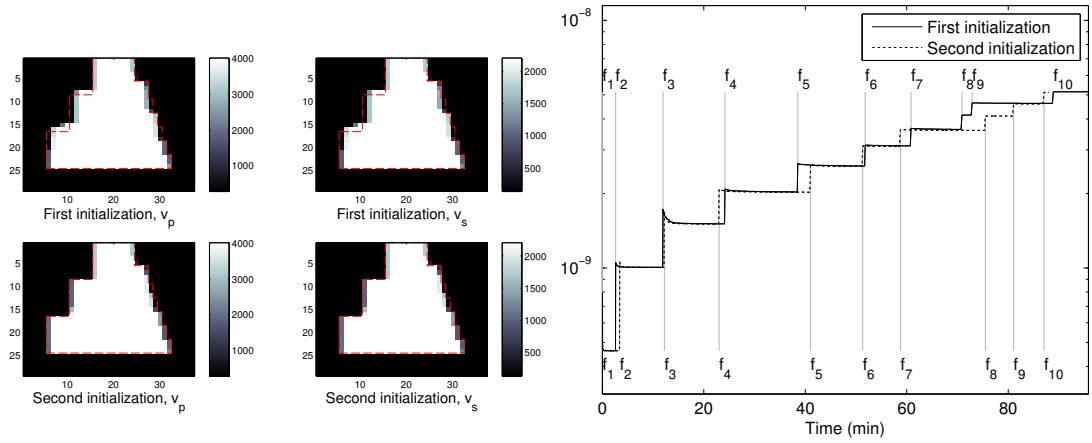

Figure 10: Results obtained with the proposed inversion scheme, $\gamma = 10^{-10}$ (left: final maps of v_p and v_s for each initialization, right: temporal evolution of the criterion)

Table 2: Computation time for the each regularization scheme and each initialization.

Regularization scheme	Initialization (i)	Initialization (ii)
Tikhonov	509 min.	1043 min.
Edge-preserving	196 min.	182 min.
Proposed method	96 min.	88 min.

3.2.1 Prior estimation of the foundation depth

In practice, the maximum error on the prior estimation of the foundation depth D is assumed to be of about 10%. We thus made several tests with varying depth estimations from 42 to 54 centimetres, the actual depth being 48 centimetres. In all cases, the algorithm was initialized by extending the top of the foundation down to the estimated depth. This corresponds to the first of the two initializations considered in the previous tests (figure 4). For each depth estimation, the final segmentation of the underground medium is presented in figure 11. We also provide the value of the data fidelity term of the criterion obtained at convergence:

$$\mathcal{J}_0(\boldsymbol{l}_l, \boldsymbol{l}_r, \varepsilon_\mathrm{p}, \varepsilon_\mathrm{s}) = \sum_\omega \sum_k \|\boldsymbol{y}_{\omega,k} - \boldsymbol{g}_{\omega,k} \circ \boldsymbol{m}(\boldsymbol{l}_l, \boldsymbol{l}_r, \varepsilon_\mathrm{p}, \varepsilon_\mathrm{s})\|^2 \tag{27}$$

The results show that the algorithm is sensitive to an inaccurate depth estimation. In particular, an underestimated (resp., overestimated) value tends to be compensated by an overestimated (resp., underestimated) foundation width.

A bad estimation of the foundation depth has also an impact on the criterion: the final value of $\mathcal{J}_0$ increases with the estimation error. To adjust the foundation depth estimate, we suggest to perform the inversion separately for several depth hypothesis and to use the value of $\mathcal{J}_0$ as an indicator of the best depth estimate.

This corresponds to a model order estimation procedure. It has been used in the framework of shape estimation in [55] where a two-dimensional boundary is described by the coefficients of a Fourier series. An unconstrained least-square criterion is minimized so that an augmentation of the model order necessarily leads to a decrease of the minimal criterion value. To regularize the problem and determine the correct model order, the authors use the Rissanen's Minimum Description Length criterion [56]. Here, the foundation width is constrained to increase with depth (assumption **A4**), which plays the role of regularization. In the unconstrained mode, a penalization term depending of the model order could be introduced in the criterion expression, akin to [56].

Another alternative would be to update the foundation depth alternatively or simultaneously with the left and right boundaries. However, it cannot be implemented without reconsidering the inversion

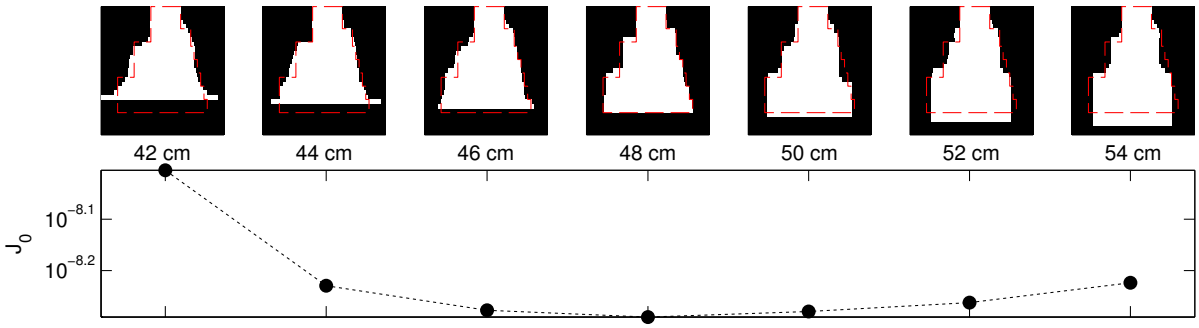

Figure 11: Robustness of the algorithm with respect to an error on the estimation of the foundation depth, $\gamma = 10^{-10}$ in each case

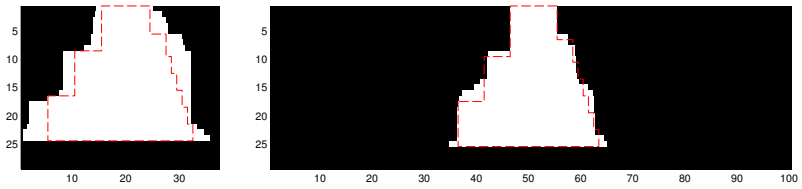

(a) (b)

Figure 12: Robustness of the algorithm with respect to an underestimation of the earth characteristics with (left) and without (right) restriction to a region of interest, $\gamma = 10^{-10}$ in the two cases

procedure. Indeed, the foundation depth determines the number of unknowns of the problem: a deeper foundation will be described by a larger number of components of $\boldsymbol{l}_l$ and $\boldsymbol{l}_r$. It thus cannot be considered as an unknown entering of the criterion in the same way as the other shape parameters.

3.2.2 Prior estimation of the earth characteristics

Here, we study the impact of an erroneous preliminary estimation of the earth characteristics. We suppose that $v_{\mathrm{p}}^{\mathrm{E}}$ and $v_{\mathrm{s}}^{\mathrm{E}}$ are set to 270 m.s^{-1} and 135 m.s^{-1} instead of 300 m.s^{-1} and 150 m.s^{-1}, respectively, which corresponds to an underestimation error of 10%. As before, the algorithm was initialized by extending the top of the foundation down to the estimated depth (first initialization in figure 4). The error on the prior estimation of the earth characteristics is taken into account in the initialization.

The final segmentation of the medium is presented in figure 12(a). The reconstruction results are significantly altered by the error on the earth characteristics estimation. We remark that an underestimation of the earth characteristics is compensated by an overestimation of the foundation width. This is mainly due to the restriction to a region of interest. Indeed, inside the region of interest, the discrepancy between the estimated and the exact velocity values is compensated by the introduction of the variables $\boldsymbol{\varepsilon}_{\mathrm{p}}$ and $\boldsymbol{\varepsilon}_{\mathrm{s}}$, whereas outside the region of interest, the underground characteristics are set to the prior estimations and the underground characteristics in this area are not part of the unknowns. Without restriction to a region of interest (figure 12(b)), the results are much closer to the exact solution. This example demonstrates that in practice, it is recommended to extend the region of interest to the whole probed area, even at the price of a higher computation cost.

3.3 Application to a configuration of realistic size

Our algorithm was finally tested on a synthetic configuration of realistic size (see figure 13). The underground medium is 9 meters and 4 meters in horizontal and vertical directions. Here, we consider that the seismic sources are detonators located in the subsurface. Each detonation produces a force field both in the horizontal and vertical directions. Figure 14 presents the seismogram resulting from the shallowest detonation on the left side of the foundation. The horizontal component (resp. the

vertical component) is represented by a 2-D Gaussian derivative along the x-axis (resp. the y-axis) with a standard deviation of Δx and Δy along the x- and y-axis respectively. The detonations occur at 18 successive locations and generate a 200 Hz Ricker wavelet. 10 frequencies from 100 Hz to 500 Hz were selected for the inversion. The measurement system consists of 44 geophones placed on the surface. White Gaussian noise is added to the simulated data (the signal to noise ratio equals 30 dB). The characteristic values of each region are those given in table 1 except that in concrete, the density ρ^{C} is now set to 2200 kg/m^3. To take into account the variation in density between earth and concrete, the segmentation of the underground medium into two regions Ω_C and Ω_E is used:

$$\boldsymbol{\rho} = \tilde{\boldsymbol{\rho}}^C \odot R^{\mathrm{C}}(\boldsymbol{l}_l, \boldsymbol{l}_r) + \tilde{\boldsymbol{\rho}}^E \odot R^{\mathrm{E}}(\boldsymbol{l}_l, \boldsymbol{l}_r) \tag{28}$$

where $\tilde{\boldsymbol{\rho}}^C$ and $\tilde{\boldsymbol{\rho}}^E$ denote prior estimations of the concrete and earth densities, respectively.

Here, the source signal is estimated during the inversion as it would be recommended in a real experiment. To initialize the algorithm, the top of the foundation is extended down to the foundation depth. We considered two cases: (1) the foundation width is supposed to increase with depth and (2) this hypothesis is not taken into account. Indeed, this assumption might not always be satisfied in practice, particularly in case of deterioration of the foundation. The final segmentations of the probed medium are presented in figure 15.

In the two cases, the estimated foundation geometry is very close to the expected result. The presented example can thus be considered as a proof of concept for the imaging of foundations. Without constraints on $\boldsymbol{l}_l$ and $\boldsymbol{l}_r$, the foundation outline is more irregular. More precisely, several "notches" are present at the basis of the estimated foundation in an erroneous way. Indeed, they appear in areas where the data sensitivity is low, because only a small fraction of the emitted waves travels forward and backward between the soil surface and the basis of the foundation, while the shape of the foundation is not regularized.

The assumption that the foundation increases with depth is not necessarily true for degraded foundations. To prevent the formation of an irregular foundation shape without taking into account this constraint, a more versatile assumption could be considered. For example, one can assume that a foundation is mainly composed of smooth edges separated by sharp transitions. In practice, one possibility is to add a regularization term function of $\boldsymbol{l}_l$ and $\boldsymbol{l}_r$ in the minimized criterion. The approximation of the total variation introduced in section 1.4.3 can be used:

$$\phi(\boldsymbol{l}_l, \boldsymbol{l}_r) = \sum_m \sqrt{([\boldsymbol{l}_l]_{m+1} - [\boldsymbol{l}_l]_m)^2 + \delta^2} + \sqrt{([\boldsymbol{l}_r]_{m+1} - [\boldsymbol{l}_r]_m)^2 + \delta^2} \tag{29}$$

Another possibility would be to introduce other constraints on the components of $\boldsymbol{l}_l$ and $\boldsymbol{l}_r$ such as:

$$[\boldsymbol{l}_l]_m \geq \min\left([\boldsymbol{l}_l]_{m-1}, [\boldsymbol{l}_l]_{m+1}\right) \tag{30}$$

$$[\boldsymbol{l}_r]_m \geq \min\left([\boldsymbol{l}_r]_{m-1}, [\boldsymbol{l}_r]_{m+1}\right) \tag{31}$$

in order to prevent the artificial notches observed on the right side of figure 15.

Conclusion

This paper tackled an inverse scattering problem for imaging a high-contrast object. The aim is to determine the geometry of a concrete foundation by means of a seismic imaging procedure. The proposed inversion procedure is based on an original description of the probed medium. It enables to take precise information into account about the shape of the scattering object and the characteristics of earth and concrete. Tests were performed on a synthetic dataset. The results revealed good performance of the proposed algorithm, contrary to more classical approaches.

As a prerequisite to real data processing, several additional tests should be performed. Firstly, tests on synthetic data could be performed on more realistic configurations. In particular, we worked on configurations where the earth and the concrete areas were supposed perfectly homogeneous. Configurations including for example a stratified underground medium could be considered. The next step would be to apply our algorithm to experimental data. In particular, it could be applied to measurements collected on a scale model, which geometrical and physical characteristics are perfectly controlled. Finally, the

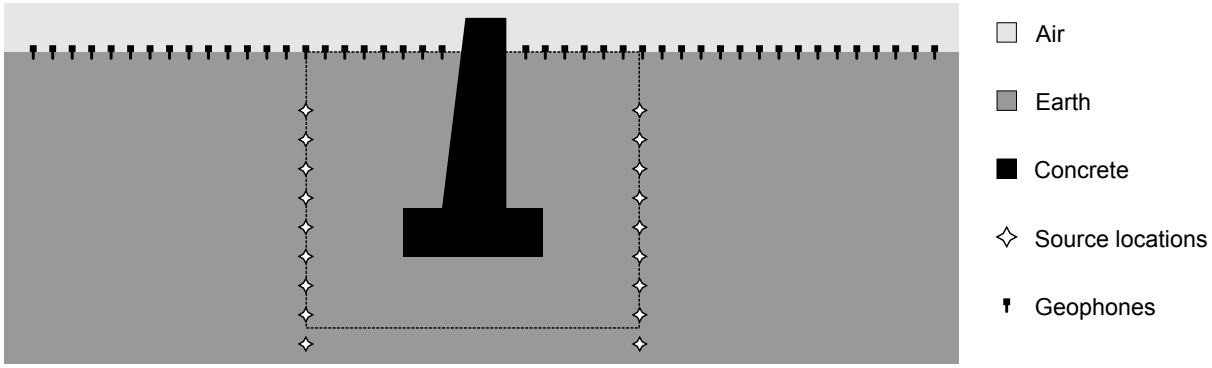

Figure 13: Scheme of the synthetic medium. The dashed line delimits the zone of interest of size 340 cm $\times$ 282 cm.

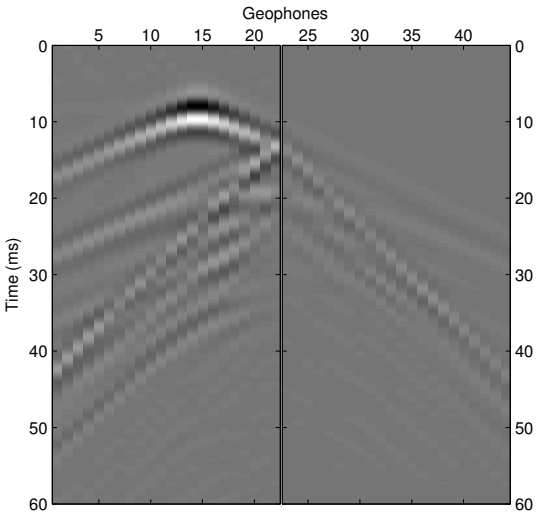

Figure 14: Seismogram resulting from the shallowest detonation on the left side of the foundation. It represents the vertical particle velocity measured by each geophone in the temporal domain.

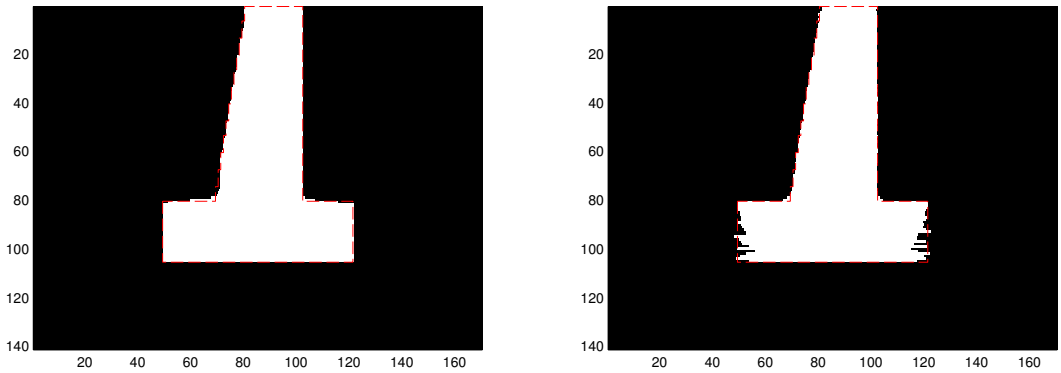

Figure 15: Results obtained on a realistic configuration. Left: the width of the foundation is supposed to increase with depth. Right: no constraint is imposed on the variation of the foundation width. $\gamma = 10^{-8}$ in the two cases.

efficiency of the proposed inversion procedure could be tested by imaging real foundations of known shapes [11].

Along with these tests, the inversion algorithm could be improved with the aim of reducing the computation time. This aspect has already been taken into account in the choice of a minimization algorithm specifically suited to large-scale nonlinear problems. However, many iterations are required, so a large number of linear systems must be solved to compute the criterion and the gradient. For this, an LU factorization is currently used. Instead of an exact factorization, an incomplete LU factorization could be performed. Provided that the theoretical convergence properties can be maintained, this would allow to strongly reduce the computational requirement, both in time and memory.

Acknowledgements

The authors thank Réseau de Transport d'Électricité - Centre National d'Expertises Réseaux for partially funding this work.

References

[1] D. Colton and R. Kress. *Inverse Acoustic and Electromagnetic Scattering Theory*. Applied Mathematical Sciences. Springer-Verlag, 2nd edition, 1998.

[2] J. A. Hudson and J. R. Heritage. The use of the Born approximation in seismic scattering problems. *Geophysical Journal International*, 66:221–240, 1981.

[3] A. J. Devaney. Inverse-scattering theory within the Rytov approximation. *Optics Letters*, 6:374–376, 1981.

[4] W.C. Chew and Y.M. Wang. Reconstruction of two-dimensional permittivity distribution using the distorted Born iterative method. *IEEE Transactions on Medical Imaging*, 9:218–225, 1990.

[5] F. Li, Q. H. Liu, and L.-P. Song. Three-dimensional reconstruction of objects buried in layered media using Born and distorted Born iterative methods. *IEEE Geoscience and Remote Sensing Letters*, 1:107–111, 2004.

[6] R. E. Kleinman and P. M. Van Den Berg. A modified gradient method for two-dimensional problems in tomography. *Journal of Computational and Applied Mathematics*, 42:17–35, 1992.

[7] P. M. Van Den Berg and R. E. Kleinman. A contrast source inversion method. *Inverse Problems*, 13:1607–1620, 1997.

[8] H. Harada, D. J. N. Wall, T. Takenaka, and M. Tanaka. Conjugate gradient method applied to inverse scattering problem. *IEEE Transactions on Antennas and Propagation*, 43:784–792, 1995.

[9] A. Franchois and C. Pichot. Microwave imaging-complex permittivity reconstruction with a Levenberg-Marquardt method. *IEEE Transactions on Antennas and Propagation*, 45:203–215, 1997.

[10] A. D. Klose and A. H. Hielscher. Quasi-Newton methods in optical tomographic image reconstruction. *Inverse Problems*, 19:387–409, 2003.

[11] O. Magnin. *Utilisation des ondes sismiques pour la caractérisation d'objets enfouis. Contribution à la mise au point d'une méthode d'imagerie sismique de trés haute résolution. Application à l'imagerie des fondations de pylônes du Réseau de Transport d'Electricité.* PhD thesis, Université Joseph Fourier – Grenoble I, 2008.

[12] P. R. Williamson. A guide to the limits of resolution imposed by scattering in ray tomography. *Geophysics*, 56:202–207, 1991.

[13] R. G. Pratt. Seismic waveform inversion in the frequency domain. Part 1: theory and verification in a physical scale model. *Geophysics*, 64:888–901, 1999.

[14] W. B. Beydoun and M. Mendes. Elastic ray-Born L2-migration/inversion. *Geophysical Journal International*, 97:151–160, 1989.

[15] A. Abubakar, W. Hu, T. M. Habashy, and P. M. Van Den Berg. Application of the finite-difference contrast-source inversion algorithm to seismic full-waveform data. *Geophysics*, 74:WCC47–WCC58, 2009.

[16] A. Askan, V. Akcelik, J. Bielak, and O. Ghattas. Full waveform inversion for seismic velocity and anelastic losses in heterogeneous structures. *The Bulletin of the Seismological Society of America*, 97:1990–2008, 2007.

[17] D. Vautrin, M. Voorons, J. Idier, Y. Goussard, S. Kerzalé, and N. Paul. Seismic imaging of transmission overhead line structure foundations. In *Computational Imaging IX (IS&T/SPIE Symposium on Electronic Imaging)*, San Francisco Airport, CA, USA, jan. 2011.

[18] Albert Tarantola. Inversion of seismic reflection data in the acoustic approximation. *Geophysics*, 49(8):1259–1266, August 1984.

[19] R. G. Pratt and M. H. Worthington. Inverse theory applied to multi-source cross-hole tomography. Part 1: acoustic wave-equation method. *Geophysical Prospecting*, 38:287–310, 1990.

[20] L. Sirgue and R. G. Pratt. Efficient waveform inversion and imaging: A strategy for selecting temporal frequencies. *Geophysics*, 69:231–248, 2004.

[21] S. Kerzalé, A. Girard, and G. D'Urso. Simulation des ondes sismiques dans la subsurface. Technical report, EDF R&D, Département STEP, 2009.

[22] E. H. Saenger, N. Gold, and S. A. Shapiro. Modeling the propagation of elastic waves using a modified finite-difference grid. *Wave Motion*, 31:77–92, 2000.

[23] D. Vautrin and M. Voorons. Régularisation et optimisation pour l'imagerie sismique des fondations de pylônes. Technical report, IRCCyN et Ecole Polytechnique de Montréal, 2010.

[24] R. Martin, D. Komatitsch, and A. Ezziani. An unsplit convolutional perfectly matched layer improved at grazing incidence for seismic wave propagation in poroelastic media. *Geophysics*, 73:T51–T61, 2008.

[25] J. Virieux and S. Operto. An overview of full-waveform inversion in exploration geophysics. *Geophysics*, 74:WCC127–WCC152, 2009.

[26] R. Brossier, S. Operto, and J. Virieux. Seismic imaging of complex onshore structures by 2D elastic frequency-domain full-waveform inversion. *Geophysics*, 74:WCC105–WCC118, 2009.

[27] E. Crase, C. Wideman, M. Noble, and A. Tarantola. Nonlinear elastic waveform inversion of land seismic reflection data. *Journal of Geophysical Research: Solid Earth*, 97:4685–4703, 1992.

[28] C. Ravaut, S. Operto, L. Improta, J. Virieux, A. Herrero, and P. Dell'Aversana. Multiscale imaging of complex structures from multifold wide-aperture seismic data by frequency-domain full-waveform tomography: application to a thrust belt. *Geophysical Journal International*, 159:1032–1056, 2004.

[29] S. Operto, J. Virieux, J.-X. Dessa, and G. Pascal. Crustal seismic imaging from multifold ocean bottom seismometer data by frequency domain full waveform tomography: application to the eastern Nankai trough. *Journal of Geophysical Research*, 111:B09306.1–33, 2006.

[30] F. Bleibinhaus, J. A. Hole, T. Ryberg, and G. S. Fuis. Structure of the California coast ranges and San Andreas fault at SAFOD from seismic waveform inversion and reflection imaging. *Journal of Geophysical Research: Solid Earth*, 112, 2007.

[31] C. Shin and Y. H. Cha. Waveform inversion in the Laplace domain. *Geophysical Journal International*, 173:922–931, 2008.

[32] P. Charbonnier, L. Blanc-Feraud, G. Aubert, and M. Barlaud. Deterministic edge-preserving regularization in computed imaging. *IEEE Transactions on Image Processing*, 6:298–311, 1997.

[33] Michael S. Zhdanov. *Geophysical inverse theory and regularization problems*. Elsevier Science, 2002.

[34] C. Gélis, J. Virieux, and G. Grandjean. Two-dimensional elastic full waveform inversion using Born and Rytov formulations in the frequency domain. *Geophysical Journal International*, 168:605–633, 2007.

[35] C. Bunks. Multiscale seismic waveform inversion. *Geophysics*, 60:1457–1473, 1995.

[36] X. Campman and C. Dwi Riyanti. Non-linear inversion of scattered seismic surface waves. *Geophysical Journal International*, 171:1118–1125, 2007.

[37] J. Nocedal and Stephen J. Wright. *Numerical Optimization*. Springer Verlag, 1999.

[38] D. Geman and C. Yang. Nonlinear image recovery with half-quadratic regularization. *IEEE Transactions on Image Processing*, 4:932–946, 1995.

[39] N. J. Carino. The impact-echo method: An overview. In *Structures Congress: A Structural Engineering Odyssey*, Washington, D.C., USA, 2001. American Society of Civil Engineers.

[40] S. J. Norton. Iterative algorithms for computing the shape of a hard scattering object: Computing the shape derivative. *Acoustical Society of America Journal*, 116:1002–1008, 2004.

[41] C. Soussen and A. Mohammad-Djafari. Polygonal and polyhedral contour reconstruction in computed tomography. *IEEE Transactions on Image Processing*, 13:1507–1523, 2004.

[42] I.T. Rekanos. Shape reconstruction of a perfectly conducting scatterer using differential evolution and particle swarm optimization. *IEEE Transactions on Geoscience and Remote Sensing*, 46:1967–1974, 2008.

[43] E.L. Miller, M. Kilmer, and C. Rappaport. A new shape-based method for object localization and characterization from scattered field data. *IEEE Transactions on Geoscience and Remote Sensing*, 38:1682–1696, 2000.

[44] M. El-Shenawee and E.L. Miller. Spherical harmonics microwave algorithm for shape and location reconstruction of breast cancer tumor. *IEEE Transactions on Medical Imaging*, 25:1258–1271, 2006.

[45] M. Li, A. Abubakar, and T.M. Habashy. A three-dimensional model-based inversion algorithm using radial basis functions for microwave data. *Antennas and Propagation, IEEE Transactions on*, 60:3361–3372, 2012.

[46] J. A. Sethian. *Level Set Methods and Fast Marching Methods: Evolving Interfaces in Computational Geometry, Fluid Mechanics, Computer Vision, and Materials Science*. Cambridge University Press, 2 edition, June 1999.

[47] S. J. Osher and R. P. Fedkiw. *Level Set Methods and Dynamic Implicit Surfaces*. Springer, 1 edition, October 2002.

[48] A. Litman, D. Lesselier, and F. Santosa. Reconstruction of a two-dimensional binary obstacle by controlled evolution of a level-set. *Inverse Problems*, 14:685–706, 1998.

[49] R. Ferraye, J.-Y. Dauvignac, and C. Pichot. An inverse scattering method based on contour deformations by means of a level set method using frequency hopping technique. *IEEE Transactions on Antennas and Propagation*, 51:1100–1113, 2003.

[50] O. Dorn and D. Lesselier. Level set methods for inverse scattering. *Inverse Problems*, 22:R67–R131, 2006.

[51] Alireza Aghasi and Justin Romberg. Sparse shape reconstruction. *SIAM Journal on Imaging Sciences*, 6:2075–2108, 2013.

[52] M. Sussman, P. Smereka, and S. Osher. A level-set approach for computing solutions to incompressible two-phase flow. *Journal of Computational Physics*, 114:146–159, 1994.

[53] H.-K. Zhao, T. Chan, B. Merriman, and S. Osher. A variational level set approach to multiphase motion. *Journal of Computational Physics*, 127:179–195, 1996.

[54] R. H. Byrd, P. Lu, J. Nocedal, and C. Zhu. A limited memory algorithm for bound constrained optimization. *SIAM Journal on Scientific Computing*, 16:1190–1208, 1995.

[55] N.A. Schmid, Y. Bresler, and P. Moulin. Complexity regularized shape estimation from noisy Fourier data. In *International Conference on Image Processing*, volume 2, pages II–453–II–456, 2002.

[56] J. Rissanen. *Stochastic Complexity in Statistical Inquiry.* World Scientific, 1998.